Nano Research

ISSN 1998-0124 CN 11-5974/O4
https://doi.org/10.1007/s12274-022-4130-z

Research Article

Highly electrically conductive graphene papers via catalytic graphitization

Huanqin Peng[1], Xin Ming[1], Kai Pang[1], Yanru Chen[1], Ji Zhou[2], Zhen Xu[1], Yingjun Liu[1,3] (✉), and Chao Gao[1] (✉)

[1] *MOE Key Laboratory of Macromolecular Synthesis and Functionalization, Department of Polymer Science and Engineering, Key Laboratory of Adsorption and Separation Materials & Technologies of Zhejiang Province, Zhejiang University, 38 Zheda Road, Hangzhou 310027, China*
[2] *Beijing Institute of Space Mechanics & Electricity, Haidian District, Beijing Friendship Road 104, Beijing 100094, China*
[3] *Shanxi-Zheda Institute of Advanced Materials and Chemical Engineering, Taiyuan 030032, China*

Received: 11 December 2021 / **Revised:** 30 November 2021 / **Accepted:** 31 December 2021

ABSTRACT

The highly electrically conductive graphene papers prepared from graphene oxide have shown promising perspectives in flexible electronics, electromagnetic interference (EMI) shielding, and electrodes. To achieve high electrical conductivity, the graphene oxide precursor usually needs to be graphitized at extremely high temperature (~ 2,800 °C), which severely increases the energy consumption and production costs. Here, we report an efficient catalytic graphitization approach to fabricate highly conductive graphene papers at lower annealing temperature. The graphene papers with boron catalyst annealed at 2,000 °C show a high conductivity of ~ 3,400 S·cm^{-1}, about 47% higher than pure graphene papers. Boron catalyst facilitates the recovery of structural defects and improves the degree of graphitization by 80%. We further study the catalytic effect of boron on the graphitization behavior of graphene oxide. The results show that the activation energy of the catalytic graphitization process is as low as 80.1 kJ·mol^{-1} in the temperature ranges studied. This effective strategy of catalytic graphitization should also be helpful in the fabrication of other kinds of highly conductive graphene macroscopic materials.

KEYWORDS

graphene papers, catalytic graphitization, boron catalyst, catalytic kinetics

1 Introduction

With the development of electronic information technology, the demand for highly electrically conductive papers is booming [1]. Compared with the widely used traditional metal foils, lightweight carbonaceous materials with high flexibility and environmental stability are considered to be good alternatives [2, 3]. Particularly, newly emerging graphene papers (GPs) have attracted strong interest from various research communities because of their excellent electrical conductivity, easy processing, and structural manipulation [4–7].

Generally, the GPs fabricated from graphene oxide (GO) dispersions by interfacial self-assembly followed by chemical reduction or thermal annealing [8, 9]. GO sheets initially have various oxygenated functional groups and structural defects on their basal plane and edges [10]. Most oxygenated functional groups could be removed by mild chemical reduction, but intrinsical lattice defects still exist, which results in poor electrically conductive performances [11]. In pursuit of highly electrically conductive GPs, chemical doping and graphitization treatment at extreme temperatures higher than 2,800 °C have been conducted in recent years [7, 11–13]. Chemical doping is an effective method to improve the electrical conductivity of GPs, but most of the doped GPs are unstable in air and high temperature environments. The graphitization process always requires extremely high temperature and long-time heat treatment, involving vast energy consumption and manufacturing costs. Moreover, the service life of the graphitization furnace would be considerably shortened at ultrahigh temperatures, which is very unfavorable for the continuous large-scale production of GPs [14]. Hence, any progress towards being able to make highly conductive GPs at temperatures below 2,800 °C is a long-term goal pursuit.

As is well known, by adding active catalysts, the activation energy of the conversion from amorphous carbon to crystalline carbon could be reduced, thus decreasing the graphitization temperature [15, 16]. The boron and its compounds have been proved to be an effective catalyst to accelerate the graphitization process of various carbonaceous materials, including pyrolytic carbon, cokes, carbon fibers, and so on [17–20]. Consequently, we have reason to believe that when incorporated with a proper boron catalyst, highly conductive GPs with a high graphitization degree could be obtained at lower thermal annealing temperature. However, no experiments have been addressed on the catalytic effect of boron on the graphitization process of GO papers.

Here, we report an efficient catalytic graphitization method to prepare highly conductive GPs at 2,000 °C, much lower than the normal graphitization temperature of 2,800 °C. The electrical conductivity of boronated GPs is up to 3,400 S·cm^{-1}, about 47% higher than that of boron-free GPs annealed at the same temperature. The excellent conductivity achieved is due to the remarkable enhancement in graphitization degree and recovery of structural defects. Furthermore, we conducted a detailed

Address correspondence to Yingjun Liu, yingjunliu@zju.edu.cn; Chao Gao, chaogao@zju.edu.cn

investigation of the effect of boron catalyst at various boron concentrations (0.1 wt.%–1 wt.%), annealing temperature (1,200–2,200 °C) and times (15–120 min) on the graphitization behavior of GO papers. The activation energy of the graphitization process is significantly decreased from 129.2 kJ·mol^{-1} of boron-free GPs to 80.1 kJ·mol^{-1} of boronated GPs.

2 Experimental section

2.1 Material preparation

Boric acid (H_3BO_3) was purchased from Aladdin Co., Ltd (Shanghai, China). Aqueous GO dispersion (Fig. S1 in the Electronic Supplementary Material (ESM)) was purchased from Hangzhou Gaoxi Technology Co. Ltd. All chemicals were used as received without further purification. Boric acid was uniformly dissolved in deionized water to prepare the boric acid solution with a mass concentration of 1.0 wt.%. The boric acid solution was added to GO dispersion to obtain homogeneous GO/H_3BO_3 dispersion with different weight percentages of boric acid (0.1 wt.%, 0.25 wt.%, 0.5 wt.% and 1.0 wt.%). The pure GO dispersion and GO/ H_3BO_3 dispersions were cast-dried at room temperature. Then, the pure GO papers and boric acid incorporated GO papers (BGO papers) were obtained by manually peeling off the PET substrate. The obtained GO papers and BGO papers were heated in a tubular furnace at 1,200 °C under Argon atmosphere for 1 h. Then, they were further annealed in graphitization furnace at 2,000 °C under Argon atmosphere obtain pure GPs and boronated GPs (BGP-0.1, BGP-0.25, BGP-0.5, BGP-1).

2.2 Characterization

X-ray photoelectron spectroscopy (XPS) (ThermoFisher ESCALAB 250Xi) was used to characterize the chemical composition and the assignments of B peaks. The detailed XPS spectra of all samples were obtained after Ar^+ ion sputtering for 1 h. The electrical conductivity was measured by a high-resolution multiple-function sourcemeter (Keithley 2460) using the four-probe method. Hall mobility and carrier density were measured on Nanometrics HL5500 Hall system. The X-ray diffraction (XRD) was performed on an X'Pert Peo diffractometer (PANalytical) using Cu Kα1 radiation with an X-ray wavelength of 1.5406 Å. Raman spectroscopy was conducted on a Renishaw in Via-Reflflex Raman microscopy with an excitation wavelength of 532 nm. The lattice of the GPs was observed using a transmission electron microscope (TEM, Hitachi H-9500). Synchronous wide-angle X-ray scattering (WAXS) was carried out in BL16B1 beamline station of Shanghai Synchrotron Radiation Facility (SSRF). The scattering patterns were collected on a CCD camera. The electromagnetic interference performance was tested by a vector network analyzer (ZNB-40, Rohde & Schwarz, Germany). The thermal analysis was performed on thermal gravimetric analysis (TGA) at a heating rate of 10 °C·min^{-1} under the nitrogen atmosphere. The mechanical performance was evaluated on a universal testing machine (Instron 2344) at a loading rate of 1.0 mm/min.

3 Results and discussion

The preparation process of pure GPs and BGPs is illustrated in Fig. 1(a). As described in the experimental section, pure GO papers and BGO papers were prepared by the solution casting method (Fig. 1(a)). After air-drying, GO papers and BGO papers were annealed at 2,000 °C under Ar atmosphere to obtain pure GPs and BGPs. Most of the oxygen-containing functional groups

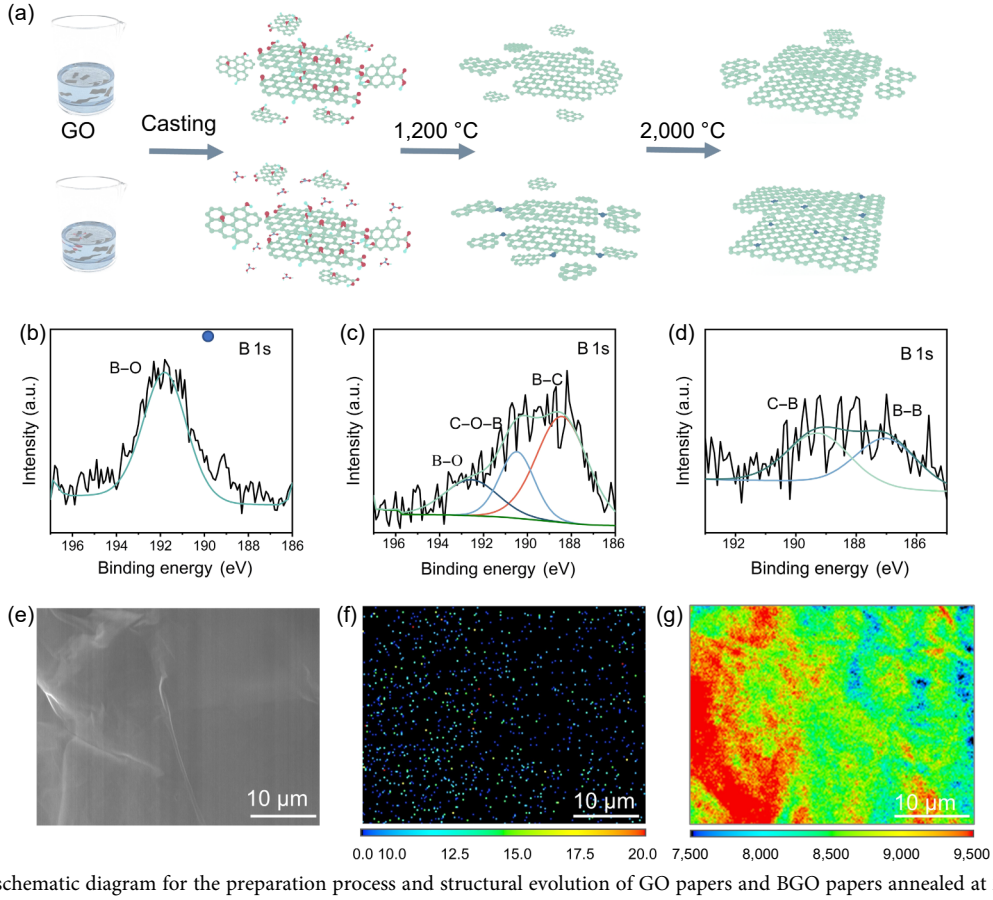

Figure 1 (a) The schematic diagram for the preparation process and structural evolution of GO papers and BGO papers annealed at 2,000 °C. (b)–(d) B 1s XPS spectra for BGO papers (b) and for BGO papers annealed at 1,200 °C (c) and 2,000 °C (d). (e)–(g) Back-scattered electron image (e) of BGPs and corresponding WDS elemental mapping for boron (f) and carbon (g).

on GO sheets are removed during annealing treatment (Fig. S2 in the ESM), while there are still abundant lattice defects and disorders that severely affect the electronic properties [21]. With the incorporation of the boric acid catalyst, the crystal structure of the BGPs becomes more complete. The BGPs show brighter silver-grey (Fig. 1(a)) and more compact graphene platelet stacking structures (Figs. S3 and S4 in the ESM), denoting higher graphitization degree and density (Fig. S4 in the ESM). The most acceptable interpretation of boron catalytic graphitization is carbon dissolution-precipitation through carbides [19, 22–24]. Specifically, boron atoms substitute the position of carbon atoms in the hexagonal rings to form carbide, then the carbides decompose and precipitate in the form of graphite at high temperature [22, 23]. Therefore, it is reasonable to infer that B_2O_3 is gradually decomposed and the boron atoms move to the substitution position to connect the ordered and disordered carbons with increasing annealing temperature. Meanwhile, the graphitic crystal is easier to grow and graphite structure gradually tends to be ordered because of the connection between ordered and disordered carbons by boron. The ordered arrangement and giant graphitic crystallites conjointly contribute to more compact structure for BGPs.

The structural evolution of boron in BGPs during the annealing process was characterized by XPS analysis (Figs. 1(b)–1(d)). The different B 1s peaks ranging from 189.0 to 193.3 eV are assigned to various oxides of boron [20, 25]. As shown in Fig. 1(b), the single strong peak at 192 eV exhibited in the BGO papers belongs to the B-O bond of boric acid. It confirms that boric acid was successfully incorporated into GO papers. After annealing at 1,200 °C, three types of boron components are distinguishable, though rather marked noise was observed due to low concentration on the surface. Besides the peak at around 192 eV, two new peaks at 190 and 188.5 eV appeared, indicating the existence of B–O–C and B–C bonds (Fig. 1(c)). For the BGPs treated at 2,000 °C, the peak of oxides of boron at 189.0–193.3 eV faded away, and the B 1s peak (Fig. 1(d)) was divided into two characteristic peaks at 188.5 and 186.9 eV, corresponding to substitutional boron atoms in graphene lattice and boron clusters, respectively [26]. As discussed above, boron mainly exists as B_2O_3 in the interspace of graphene at lower annealing temperature. With increasing annealing temperature, the B_2O_3 begins to decompose and boron atoms gradually diffuse into the interstitial position and substitution position [19]. To further analyze the distribution of B element, the electron probe microanalyzer (EPMA) was used to scan B signal in a wide range by the wavelength-dispersive spectroscopy (WDS) mapping analysis (Figs. 1(e)–1(g)). The WDS elemental distribution map of boron (Fig. 1(f)) demonstrates the homogeneous distribution of B atoms without aggregation in BGPs.

Raman spectroscopy is an effective technique to characterize the structural defects of graphene materials. It is well-known that the D band (1,330–1,350 cm^{-1}) is a characteristic peak of cavity defects and topological defects in graphene layers [27]. G band (1,580–1,600 cm^{-1}) is associated with the complete sp^2-hybridized carbon-carbon bonds in carbon materials [28, 29]. The Raman spectra of pure GPs and BGPs with different boron contents are shown in Fig. 2(a). All samples exhibit a similar peak position after annealing at 2,000 °C. The intensity ratio of I_D/I_G was calculated to quantitatively assess the degree of structural integrity in the graphene layers. As shown in Fig. 2(b), the value of I_D/I_G

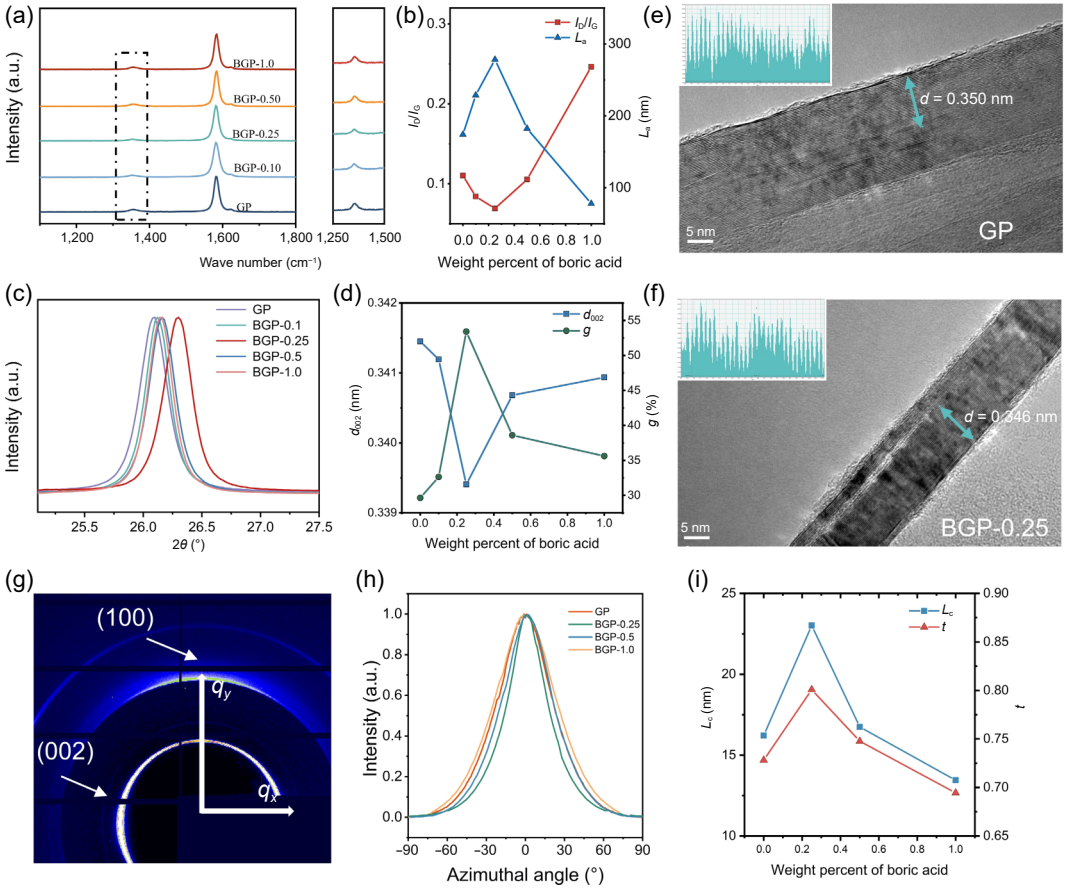

Figure 2 (a) Raman spectra of pure GPs and BGPs annealed at 2,000 °C. (b) Raman peak ratio of I_D/I_G and calculated L_a of pure GPs and BGPs. (c) XRD patterns of pure GPs and BGPs annealed at 2,000 °C. (d) Effect of boron content on the interlayer distance and degree of graphitization of pure GPs and BGPs. TEM images of GP (e) and BGP-0.25 (f). (g) WAXS patterns of BGP-0.25 (h) Azimuthal scan curves from WAXS. (i) Effect of boron content on the crystalline size (L_c) and orientation degree (*f*).

decreased with boroncontent from 0.11 wt.% of 0 wt.% to 0.06 wt.% of 0.25 wt.%, and then gradually increased to 0.25 when the boron content increased to 1 wt.%. The extremely low I_D/I_G of BGP-0.25 indicates moderate boron content (up to 0.25 wt.%) has a positive catalytic effect on the graphitization of GO. However, it shows a reverse effect at higher concentrations due to surface flaws etched by B_2O_3 decomposition and impurity effect of the heteroatoms [18, 30–31]. Furthermore, the lateral size (L_a) of graphene lattice in GPs could be estimated according to the Eq. [13]

$$L_a = C(\lambda)/(I_D/I_G) \quad (1)$$

where $C(\lambda)$ is a constant of 4.4. The L_a of BGP-0.25 was estimated to be 278 nm, 1.6 times higher than that of pure GPs under the same annealing temperature. This denotes that the boron catalyst with a proper content effectively promotes the structure evolution of graphite crystallite in GPs during the annealing process.

The Raman spectra results indicate that the incorporation of boron contributes to the formation of graphitic crystal structure in GPs at lower annealing temperature. Therefore, we further investigated the parameters of crystal structure, including the interlayer spacing (d_{002}) and degree of graphitization (g) of each sample by XRD profiles in detail. All samples show a sharp single (002) reflection peak at ~ 26°, which correlates with the (002) crystal lattice of graphite (Fig. 2(c)). Usually, when the g increased gradually, the (002) peak shifted right, and the (002) peak profile became sharper and more symmetrical [32]. The d_{002} and g could be calculated from XRD spectra according to the equations as follows [33, 34]

$$d_{002} = \frac{\lambda}{2\sin\theta} \quad (2)$$

$$g = \frac{3.44 - d_{002}}{3.44 - 3.345} \times 100\% \quad (3)$$

where λ is radiation wavelength; θ is the angular position of the peak; 3.44 is the interlayer distance of turbostratic graphite, Å; 3.354 is the interlayer distance for ideal perfect graphite, Å.

When the weight percentage of boric acid was below 0.25 wt.%, the (002) peaks of BGPs shifted to a higher angle with the increment of boron content, demonstrating that the g of the BGPs was significantly improved through boron catalytic graphitization (Fig. 2(d)) [18]. The samples of pure GP and BGP-0.25 display sharp peaks at 26.08° and 26.30°, and the corresponding graphitization degree is 29.64% and 53.41%, respectively. This confirms boron acid is an effective catalyst to promote the graphitization process and reduce the thermal annealing temperature for GO.

It also could be observed from the TEM images of GP (Fig. 2(e)) and BGP-0.25 (Fig. 2(f)). The interlayer distance of BGP-0.25 is 0.346 nm, lower than that (0.350 nm) of pure GPs, which is basically consistent with the results of XRD spectra (Figs. 2(c) and 2(d)). Furthermore, WAXS was conducted to characterize the internal crystallites of GPs in the transmission model. The scattering intensities of (002) and (001) peaks of BGP-0.25 are stronger than those of pure GP (Fig. S5 in the ESM). The average thickness (L_c) of crystallites in the (002) direction could be evaluated according to the Scherrer equation [33]

$$L_c = 0.9\lambda/(\beta\cos\theta) \quad (4)$$

where λ is the X-ray wavelength and β is the full width at half-maximum for the (002) peak obtained by radial scanning at q_x direction in WAXS patterns (Fig. S6 in the ESM). The calculation result shows that BGP-0.25 holds the largest L_c up to 23 nm, much larger than that of pure GPs (~ 16 nm) and those of BGPs with higher boron contents (Fig. 2(i)). The orientation degree can be calculated from the azimuthal scanning integral curves (Fig. 2(h)). The WAXS result demonstrates that the orientation degree was improved from 0.73 of pure GP to 0.8 of BGP-0.25, indicating a more ordered and compact structure (Fig. 2(i)).

Both Raman and XRD spectra demonstrate that moderate boron incorporation can effectively repair structural defects and facilitate the formation of relatively large crystalline domains in GPs. To further study the effect of boron on the catalysis of graphitization of GO, we tracked the XRD evolution of pure GO paper and BGO papers with 0.25 wt.% boric acid that annealed at 2,000 and 2,200 °C for different times (15–120 min). All the (002) peaks shift towards a higher angle with the extension of annealing time (Figs. 3(a) and 3(b)). This phenomenon indicates that the interlayer distance of graphene layers (d_{002}) gradually decreases and the graphitization degree (g) improves with annealing time (Fig. S7 in the ESM). The degree of disorder (P=1–g) has been

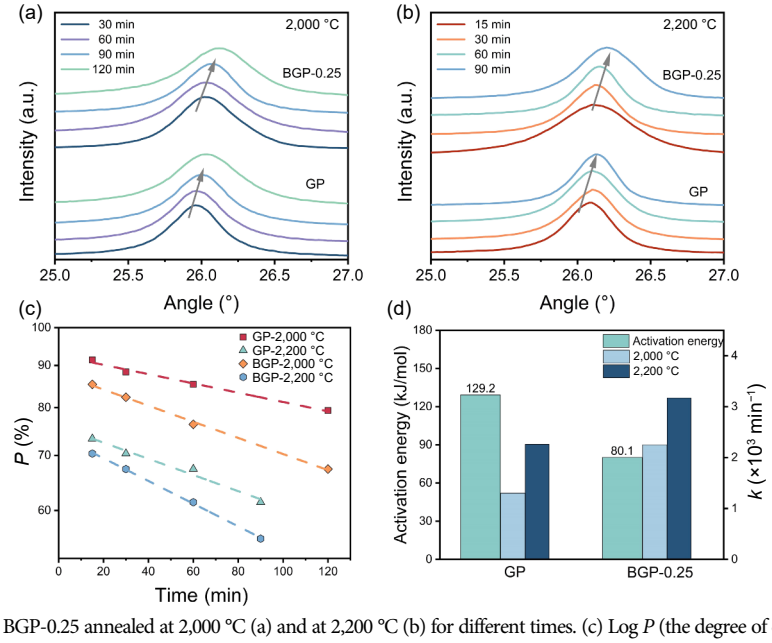

Figure 3 XRD curves of GP and BGP-0.25 annealed at 2,000 °C (a) and at 2,200 °C (b) for different times. (c) Log P (the degree of disorder) versus annealing time for GP and BGP-0.25. (d) Activation energy and specific rate constant of GP and BGP-0.25 at 2,000 and 2,200 °C.

employed to calculate the kinetic parameter [35]. The value of P may be considered as a measure of the fraction of GPs, which remains to be graphitized. The kinetic change of P is presented in the form of Log P against annealing time for GP and BGP-0.25 (Fig. 3(c)). The catalytic graphitization of GO could be regarded as a first-order reaction because the slope of the curve is constant during a period of time [34]. The rate constant k and activation energy (E_a) of graphitization at a certain temperature could be obtained by calculating the first-order equation and Arrhenius equation, respectively [35]

$$kt = Ln\frac{P_0}{P} \quad (5)$$

$$Ln(k) = -\frac{E_a}{RT} + C \quad (6)$$

where P is the degree of disorder, k is kinetic reaction rate constant, E_a is the activation energy, R is the universal gas constant, and T is the absolute temperature. The activation energy of the graphitization process calculated from the Arrhenius equation are 129.2 and 80.1 kJ·mol^{-1} for pure GO and BGO, respectively (Fig. 3(d)). The obtained activation energy of graphitization is much lower than that of pyrolytic carbons and petroleum coke, which may be ascribed to the size difference in starting materials, particularly the lateral size [36]. The reaction rate constant of graphitization at 2,000 °C is 1.3×10^{-3} and 2.25×10^{-3} min^{-1} for GP and BGP-0.25, respectively. The lower activation energy and higher rate constant means that boron incorporation could accelerate the rate of graphitization of GO and reduce the graphitization temperature [37].

The electrical conductivity of GPs is closely relevant to the crystallite size and graphitization degree of GPs. Hence, we speculate boron incorporation could effectively improve the electrical conductivity of GPs. The conductivity of GPs and BGPs was measured by the standard four-probe method and acquired via calculating the slope of I–V curves (Fig. 4(a) and Fig. S8 in the ESM). The effect of boric acid concentration on the electrical conductivity of BGPs is consistent with the effect on the crystallite size (Fig. 2(b), i) and graphitization degree (Fig. 2(d)). The BGP-0.25 shows the highest electrical conductivity of 3,400 S·cm^{-1}, which is about 47% higher than that of pure GPs. For the BGPs with boron content higher than 0.25 wt.%, excessive boron loading accelerates the generation of defects and the occupation in interstitial positions [19]. Meanwhile, numerous surface flaws are etched by B_2O_3 decomposition, as confirmed by Raman (Figs. 2(a) and 2(b)). Therefore, the electrical conductivity of BGP with high boron loading sharply dropped. The conductivity of BGP-0.25 surpasses those of GPs annealed at 2,000 °C reported previously, even comparable to that of pure GPs annealed at 2,800 °C (Fig. 4(b)) [8, 38–43].

To further study the mechanism for considerable improvement in electrical conductivity, Hall effect measurement was conducted in a commonly used van der Pauw geometry. The carrier mobility increases with the boron content from 411 cm^2·V^{-1}·S^{-1} (pure GP) to 615 cm^2·V^{-1}·S^{-1} (BGP-0.25), which is also consistent with the trend of graphitization degree. For BGPs with boron content higher than 0.25 wt.%, the drop in carrier mobility is because the heat treatment process can produce some defects in graphene crystallites and the B atoms are charged-impurity scatterers to limit the carrier transport [44, 45]. The improvement of electrical conductivity is mainly attributed to the increased carrier mobility (or graphitization degree) (Fig. S9 in the ESM) because the carrier density of BGPs basically remains unchanged when the boron content lower than 0.5 wt.% (Fig. 4(c)). With the incorporation of the boric acid catalyst, the degree of graphitization improves and crystal structure of the BGPs becomes more complete, which is conducive to the improvement of mobility [39].

Generally, carbon-based materials with higher electrical conductivity exhibit better electromagnetic interference (EMI) shielding effectiveness (SE) [46]. As shown in Fig. 4(d), compared with pure GPs, the EMI shielding performances of all BGPs are significantly improved, which further verified our previous results. The SE of the BGP-0.25 with the thickness of 16 μm notably increased from 62.67–61.11 to 66.90–66.13 dB in 8–12 GHz. The increment of electrical conductivity is mainly responsible for the improvement in EMI shielding performance [39]. To further investigate the shielding mechanism, reflection SE (SE_R) and absorption SE (SE_A) as well as the coefficient of reflection (R), absorption (A), and transmission (T) in pure GP and BGP-0.25 were calculated (Fig. S10 and Table S1 in the ESM). The reflection coefficient is higher than absorption coefficient for both GP and BGPs, suggesting that they are highly reflective materials [47]. However, the SE_A is much higher than the SE_R for both GP and BGP-0.25, indicating the absorption is the dominant shielding

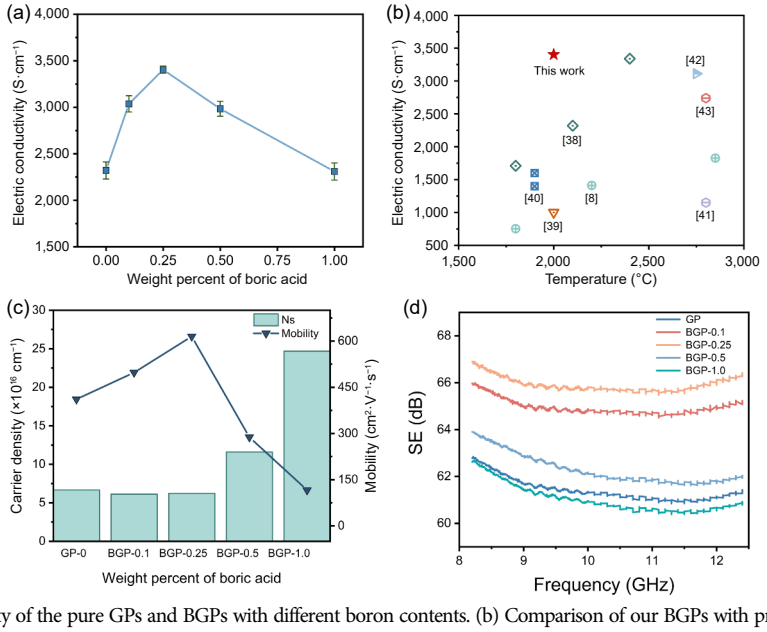

Figure 4 (a) Electrical conductivity of the pure GPs and BGPs with different boron contents. (b) Comparison of our BGPs with previously reported GPs in terms of electrical conductivity and annealing temperature. (c) Hall effect measurements of carrier density and mobility of GPs and BGPs. (d) The SE of pure GP and BGPs.

mechanism. The SE_A of GP and BGP-0.25 are 43.6 and 52.6 dB, respetively. Therefore, the improvement of EMI shielding performance is mainly attributed to increment of SE_A after boron incorporation [48]. These results also denote that annealing BGPs at a relatively low temperature of 2,000 °C is an alternative preparation method for high-performance EMI shielding materials.

We also assessed the oxidation resistance and mechanical properties of pure GPs and BGPs. The results of TGA confirmed that the oxidation rate of GPs was drastically reduced, and the thermal decomposition temperature was greatly increased from 718 to 761 °C after boron catalytic graphitization (Fig. S11 in the ESM). The tensile strength and modulus improve with moderate boron incorporation, reaching maximums of 39 and 830 MPa, respectively, at 0.25 wt.% content of boron acid (Fig. S12 in the ESM). With further increment of boron loading, more defects are generated by the excessive boron, leading to the drop in both the tensile strength and modulus.

4 Conclusions

We demonstrate that adding boric acid as a catalyst is an energy-saving and effective method to fabricate highly conductive GPs. The results of Raman spectra and XRD spectra confirm that boron can repair structural defects and improve the graphitization degree for GPs at a lower annealing temperature. Furthermore, the catalytic kinetics indicates that boron incorporation can significantly decrease the activation energy and accelerate the rate of the graphitization process. The electrical conductivity of BGPs is 3,400 $S \cdot cm^{-1}$, and the graphitization degree is 53%, much higher than pure GPs annealed at the same temperature. Hence, the catalytic graphitization is an efficient approach to decreaseing the graphitization temperature and dramatically reduce the production cost, making it possible for wide applications in graphene-based flexible electronics, EMI shielding and electrodes.

Acknowledgements

This work is supported by the National Natural Science Foundation of China (Nos. 51803177, 52090030, and 52106071), the Fundamental Research Funds for the Central Universities, Shanxi-Zheda Institute of New Materials and Chemical Engineering (No. 2012SZ-FR004), Key Laboratory of Novel Adsorption and Separation Materials and Application Technology of Zhejiang Province (No. 512301-I21502). The authors thank the members of staff at SSRF for synchronous WAXS characterizations.

Electronic Supplementary Material: Supplementary material (further details of the SEM images, XPS spectra, TGA curves, etc.) is available in the online version of this article at https://doi.org/10.1007/s12274-022-4130-z.

References

[1] Liu, Y. J.; Yang, M. C.; Pang, K.; Wang, F.; Xu, Z.; Gao, W. W.; Gao, C. Environmentally stable macroscopic graphene films with specific electrical conductivity exceeding metals. *Carbon* **2020**, *156*, 205–211.

[2] Yamada, Y.; Chung, D. D. L. Epoxy-based carbon films with high electrical conductivity attached to an alumina substrate. *Carbon* **2008**, *46*, 1798–1801.

[3] Liu, Y. J.; Li, P.; Wang, F.; Fang, W. Z.; Xu, Z.; Gao, W. W.; Gao, C. Rapid roll-to-roll production of graphene films using intensive joule heating. *Carbon* **2019**, *155*, 462–468.

[4] Lin, S. F.; Ju, S.; Zhang, J. W.; Shi, G.; He, Y. L.; Jiang, D. Z. Ultrathin flexible graphene films with high thermal conductivity and excellent Emi shielding performance using large-sized graphene oxide flakes. *RSC Adv.* **2019**, *9*, 1419–1427.

[5] Peng, L.; Xu, Z.; Liu, Z.; Guo, Y.; Li, P.; Gao, C. Ultrahigh thermal conductive yet superflexible graphene films. *Adv. Mater.* **2017**, *29*, 1700589.

[6] Zhang, M.; Wang, Y. L.; Huang, L.; Xu, Z. P.; Li, C.; Shi, G. Q. Multifunctional pristine chemically modified graphene films as strong as stainless steel. *Adv. Mater.* **2015**, *27*, 6708–6713.

[7] Pang, K.; Liu, X. T.; Liu, Y. J.; Chen, Y. R.; Xu, Z.; Shen, Y.; Gao, C. Highly conductive graphene film with high-temperature stability for electromagnetic interference shielding. *Carbon* **2021**, *179*, 202–208.

[8] Xin, G. Q.; Sun, H. T.; Hu, T.; Fard, H. R.; Sun, X.; Koratkar, N.; Borca-Tasciuc, T.; Lian, J. Large-area freestanding graphene paper for superior thermal management. *Adv. Mater.* **2014**, *26*, 4521–4526.

[9] Gómez-Navarro, C.; Burghard, M.; Kern, K. Elastic properties of chemically derived single graphene sheets. *Nano Lett.* **2008**, *8*, 2045–2049.

[10] Geim, A. K.; Novoselov, K. S. The rise of graphene. In *Nanoscience and Technology*. Rodgers, P., Ed.; Co-Published with Macmillan Publishers Ltd: London, 2009; pp 11–19.

[11] Liu, Y. J.; Xu, Z.; Zhan, J. M.; Li, P. G.; Gao, C. Superb electrically conductive graphene fibers via doping strategy. *Adv. Mater.* **2016**, *28*, 7941–7947.

[12] Song, R. G.; Wang, Q. L.; Mao, B. Y.; Wang, Z.; Tang, D. L.; Zhang, B.; Zhang, J. W.; Liu, C. G.; He, D. P.; Wu, Z. et al. Flexible graphite films with high conductivity for radio-frequency antennas. *Carbon* **2018**, *130*, 164–169.

[13] Abakumov, A. A.; Bychko, I. B.; Nikolenko, A. S.; Strizhak, P. E. Dependence of structure of multilayer graphene oxide on degree of graphitization of initial graphite. *Theoret. Exp. Chem.* **2018**, *54*, 186–192.

[14] Bahl, O. P.; Mathur, R. B.; Gupta, D. A novel method of improving the Young's modulus of carbon fibres. *Fibre Sci. Technol.* **1982**, *17*, 149–153.

[15] Zha, Z. T.; Zhang, Z.; Xiang, P.; Zhu, H. Y.; Zhou, B. M.; Sun, Z. L.; Zhou, S. One-step preparation of eggplant-derived hierarchical porous graphitic biochar as efficient oxygen reduction catalyst in microbial fuel cells. *RSC Adv.* **2021**, *11*, 1077–1085.

[16] Destyorini, F.; Yudianti, R.; Irmawati, Y.; Hardiansyah, A.; Hsu, Y. I.; Uyama, H. Temperature driven structural transition in the nickel-based catalytic graphitization of coconut coir. *Diam. Relat. Mater.* **2021**, *117*, 108443.

[17] Chen, L.; Fang, T.; Song, C. Y.; Li, H. L.; Hu, J. Catalytic graphitization of boron on the fabrication of high-performance carbon papers for gas diffusion layers in PEMFCs. *Catal. Commun.* **2021**, *157*, 106332.

[18] Jones, L. E.; Thrower, P. A. Influence of boron on carbon fiber microstructure, physical properties, and oxidation behavior. *Carbon* **1991**, *29*, 251–269.

[19] Wen, Y.; Lu, Y. G.; Xiao, H.; Qin, X. Y. Further investigation on boric acid catalytic graphitization of polyacrylonitrile carbon fibers: Mechanism and mechanical properties. *Mater. Des.* **2012**, *36*, 728–734.

[20] Burgess, J. S.; Acharya, C. K.; Lizarazo, J.; Yancey, N.; Flowers, B.; Kwon, G.; Klein, T.; Weaver, M.; Lane, A. M.; Heath Turner, C. et al. Boron-doped carbon powders formed at 1,000 °C and one atmosphere. *Carbon* **2008**, *46*, 1711–1717.

[21] De Silva, K. K. H.; Huang, H. H.; Joshi, R.; Yoshimura, M. Restoration of the graphitic structure by defect repair during the thermal reduction of graphene oxide. *Carbon* **2020**, *166*, 74–90.

[22] Zhang, F. Y.; He, D. M.; Ge, S. T.; Cai, Q. Y. Effect of fiber splitting on the catalytic graphitization of electroless Ni-B-coated polyacrylonitrile-based carbon fibers. *Surf. Coat. Technol.* **2008**, *203*, 99–103.

[23] Agrawal, A.; Yinnon, H.; Uhlmann, D. R.; Pepper, R. T.; Desper, C. R. Boron modification of carbon fibres. *J. Mater. Sci.* **1986**, *21*, 3455–3466.

[24] Chen, H. J.; Yang, J. X.; Shuai, Q.; Li, J.; Ouyang, Q.; Zhang, S. In-

situ doping B_4C nanoparticles in pan precursors for preparing high modulus pan-based carbon fibers with boron catalytic graphitization. *Compos. Sci. Technol.* **2020**, *200*, 108455.

[25] Cermignani, W.; Paulson, T. E.; Onneby, C.; Pantano, C. G. Synthesis and characterization of boron-doped carbons. *Carbon* **1995**, *33*, 367–374.

[26] Kim, E.; Oh, I.; Kwak, J. Atomic structure of highly ordered pyrolytic graphite doped with boron. *Electrochem. Commun.* **2001**, *3*, 608–612.

[27] Gupta, A.; Chen, G.; Joshi, P.; Tadigadapa, S.; Eklund N. Raman scattering from high-frequency phonons in supported n-graphene layer films. *Nano Lett.* **2006**, *6*, 2667–2673.

[28] Ferrari, A. C.; Meyer, J. C.; Scardaci, V.; Casiraghi, C.; Lazzeri, M.; Mauri, F.; Piscanec, S.; Jiang, D.; Novoselov, K. S.; Roth, S. et al. Raman spectrum of graphene and graphene layers. *Phys. Rev. Lett.* **2006**, *97*, 187401.

[29] Ni, Z.; Wang, Y.; Yu, T.; Shen, Z. Raman spectroscopy and imaging of graphene. *Nano Res.* **2008**, *1*, 273–291.

[30] Kim, Y. A.; Fujisawa, K.; Muramatsu, H.; Hayashi, T.; Endo, M.; Fujimori, T.; Kaneko, K.; Terrones, M.; Behrends, J.; Eckmann, A. et al. Raman spectroscopy of boron-doped single-layer graphene. *ACS Nano* **2012**, *6*, 6293–6300.

[31] Li, X. Y.; Wang, X. P.; Xiao, G. Z.; Zhu, Y. Identifying active sites of boron, nitrogen co-doped carbon materials for the oxygen reduction reaction to hydrogen peroxide. *J. Colloid Interf. Sci.* **2021**, *602*, 799–809.

[32] Ōya, A.; Yamashita, R.; Ōtani, S. Catalytic graphitization of carbons by borons. *Fuel* **1979**, *58*, 495–500.

[33] Feret, F. R. Determination of the crystallinity of calcined and graphitic cokes by X-ray diffraction. *Analyst* **1998**, *123*, 595–600.

[34] Yokokawa, C.; Hosokawa, K.; Takegami, Y. A kinetic study of catalytic graphitization of hard carbon. *Carbon* **1967**, *5*, 475–480.

[35] Murty, H. N.; Biederman, D. L.; Heintz, E. A. Kinetics of graphitization-I. Activation energies. *Carbon* **1969**, *7*, 667–681.

[36] Noda, T.; Inagaki, M.; Sekiya, T. Kinetic studies of the graphitization process—I Effect of ambient gas phase on the rate of graphitization. *Carbon* **1965**, *3*, 175–180.

[37] Murty, H. N.; Biederman, D. L.; Heintz, E. A. Apparent catalysis of graphitization. 3. Effect of boron. *Fuel* **1977**, *56*, 305–312.

[38] Rozada, R.; Paredes, J. I.; Villar-Rodil, S.; Martínez-Alonso, A.; Tascón, J. M. D. Towards full repair of defects in reduced graphene oxide films by two-step graphitization. *Nano Res.* **2013**, *6*, 216–233.

[39] Shen, B.; Zhai, W. T.; Zheng, W. G. Ultrathin flexible graphene film: An excellent thermal conducting material with efficient emi shielding. *Adv. Funct. Mater.* **2014**, *24*, 4542–4548.

[40] Ghosh, T.; Biswas, C.; Oh, J.; Arabale, G.; Hwang, T.; Luong, N. D.; Jin, M. H.; Lee, Y. H.; Nam, J. D. Solution-processed graphite membrane from reassembled graphene oxide. *Chem. Mater.* **2012**, *24*, 594–599.

[41] Ding, J. H.; Ur Rahman, O.; Zhao, H. R.; Peng, W. J.; Dou, H. M.; Chen, H.; Yu, H. B. Hydroxylated graphene-based flexible carbon film with ultrahigh electrical and thermal conductivity. *Nanotechnology* **2017**, *28*, 39LT01.

[42] Chen, Y. N.; Fu, K.; Zhu, S. Z.; Luo, W.; Wang, Y. B.; Li, Y. J.; Hitz, E.; Yao, Y. G.; Dai, J. Q.; Wan, J. et al. Reduced graphene oxide films with ultrahigh conductivity as li-ion battery current collectors. *Nano Lett.* **2016**, *16*, 3616–3623.

[43] Zhou, E. Z.; Xi, J. B.; Guo, Y.; Liu, Y. J.; Xu, Z.; Peng, L.; Gao, W. W.; Ying, J.; Chen, Z. C.; Gao, C. Synergistic effect of graphene and carbon nanotube for high-performance electromagnetic interference shielding films. *Carbon* **2018**, *133*, 316–322.

[44] Dresselhaus, M. S.; Dresselhaus, G. Intercalation compounds of graphite. *Adv. Phys.* **2002**, *51*, 1–186.

[45] Chen, S. H.; Nguyen, Y.; Chen, T. W.; Yen, Z. L.; Hofmann, M.; Hsieh, Y. P. Neutral scatterers dominate carrier transport in CVD graphene with ionic impurities. *Carbon* **2020**, *165*, 163–168.

[46] Iwashita, N.; Inagaki, M.; Hishiyama, Y. Relations between degree of graphitization and galvanomagnetic properties of pyrolytic carbons and cokes. *Carbon* **1997**, *35*, 1073–1077.

[47] Wei, Q. W.; Pei, S. F.; Qian, X. T.; Liu, H. P.; Liu, Z. B.; Zhang, W. M.; Zhou, T. Y.; Zhang, Z. C.; Zhang, X. F.; Cheng, H. M. et al. Superhigh electromagnetic interference shielding of ultrathin aligned pristine graphene nanosheets film. *Adv. Mater.* **2020**, *32*, 1907411.

[48] Wan, S. J.; Chen, Y.; Fang, S. L.; Wang, S. J.; Xu, Z. P.; Jiang, L.; Baughman, R. H.; Cheng, Q. F. High-strength scalable graphene sheets by freezing stretch-induced alignment. *Nat. Mater.* **2021**, *20*, 624–631.